Southern Ocean drives multi-decadal atmospheric CO2 rise during Heinrich Stadials

PNAS RESEARCH ARTICLE | EARTH, ATMOSPHERIC, AND PLANETARY SCIENCES OPEN ACCESS

Southern Ocean drives multidecadal atmospheric CO_2 rise during Heinrich Stadials

Kathleen A. Wendt[a,1], Christoph Nehrbass-Ahles[b,c], Kyle Niezgoda[a], David Noone[a], Michael Kalk[a], Laurie Menviel[d], Julia Gottschalk[e], James W. B. Rae[f], Jochen Schmitt[b], Hubertus Fischer[b], Thomas F. Stocker[b], Juan Muglia[g], David Ferreira[h], Shaun A. Marcott[i], Edward Brook[a], and Christo Buizert[a]

Edited by Jeffrey Severinghaus, University of California San Diego Scripps Institution of Oceanography, La Jolla, CA; received November 8, 2023; accepted March 28, 2024

The last glacial period was punctuated by cold intervals in the North Atlantic region that culminated in extensive iceberg discharge events. These cold intervals, known as Heinrich Stadials, are associated with abrupt climate shifts worldwide. Here, we present CO_2 measurements from the West Antarctic Ice Sheet Divide ice core across Heinrich Stadials 2 to 5 at decadal-scale resolution. Our results reveal multi-decadal-scale jumps in atmospheric CO_2 concentrations within each Heinrich Stadial. The largest magnitude of change (14.0 ± 0.8 ppm within 55 ± 10 y) occurred during Heinrich Stadial 4. Abrupt rises in atmospheric CO_2 are concurrent with jumps in atmospheric CH_4 and abrupt changes in the water isotopologs in multiple Antarctic ice cores, the latter of which suggest rapid warming of both Antarctica and Southern Ocean vapor source regions. The synchroneity of these rapid shifts points to wind-driven upwelling of relatively warm, carbon-rich waters in the Southern Ocean, likely linked to a poleward intensification of the Southern Hemisphere westerly winds. Using an isotope-enabled atmospheric circulation model, we show that observed changes in Antarctic water isotopologs can be explained by abrupt and widespread Southern Ocean warming. Our work presents evidence for a multi-decadal- to century-scale response of the Southern Ocean to changes in atmospheric circulation, demonstrating the potential for dynamic changes in Southern Ocean biogeochemistry and circulation on human timescales. Furthermore, it suggests that anthropogenic CO_2 uptake in the Southern Ocean may weaken with poleward strengthening westerlies today and into the future.

ice core | paleoclimate | carbon cycle | Heinrich Stadials | carbon dioxide

Significance

Earth's climate system and carbon cycle interact in myriad ways that can add or remove CO_2 from the atmosphere. We use Antarctic ice cores to resolve four multi-decadal-scale CO_2 rises of up to 14 ppm that occurred during the most recent glacial period. These abrupt rises coincide with cold periods and iceberg discharge in the North Atlantic. Ice cores show synchronous abrupt warming in Antarctica and vapor source regions, which is consistent with increasing Southern Ocean ventilation due to shifting Southern Hemisphere westerly winds. Our results highlight past periods of dynamic changes in Southern Ocean biogeochemistry and circulation that occurred on human timescales and suggest that Southern Ocean CO_2 uptake may weaken as Southern Hemisphere westerlies strengthen in the future.

The last glacial period was punctuated by millennial-scale cold intervals in the northern hemisphere (NH), referred to as stadials. A Heinrich Stadial (HS) is defined as a stadial that culminated in a rapid and extensive ice rafting event in the North Atlantic, known as a Heinrich Event (HE) (1–3). The unique impacts of these century-scale ice-rafting events and the HS they occurred in have been identified in paleoclimate records worldwide (4). A key mechanism that facilitated the global propagation of these impacts was a weakening of the Atlantic Meridional Overturning Circulation (AMOC) during NH stadials (5, 6), which amplified the interhemispheric temperature contrast through an oceanic teleconnection known as the thermal bipolar seesaw (7, 8). During all stadials (Heinrich and non-Heinrich alike), synchronous decreases in global methane (CH_4) concentrations (9), rainfall decrease in the NH subtropics (10, 11), and rainfall increase in the Southern Hemisphere (SH) subtropics (12) have been linked to southward shifts in the Intertropical Convergence Zone (ITCZ) in response to northern high-latitude temperature perturbations (13, 14). Unlike non-Heinrich stadials, HSs are characterized by an abrupt rise in CH_4 of the order of ~10s ppb that occurred within the millennial-scale cold interval of low CH_4 (15). These short-lived CH_4 peaks within HSs coincide with maximum wet conditions in the SH subtropics (16) and are attributed to an expansion of SH subtropical wetland emissions due to a maximum southerly displacement of the ITCZ in response to a North Atlantic HE (15).

Abrupt rises in atmospheric carbon dioxide (CO_2), also referred to as carbon dioxide jumps or CDJs (17), have been found during HS-1 (18), HS-4, and HS-5 (19–21). The timing of each jump is within dating uncertainty of the HE that occurred during each HS, as previously observed in high-resolution CH_4 records (15). For example, the beginning of HE 1 (16.2 ka B.P., where "present" is the year 1950) (22) shows a CO_2 jump of 12 ± 1 ppm within the span of a century, coinciding with a ~40 ppb spike in CH_4 measured in the same ice core (15, 18). Evidence for comparable CO_2 jumps of ~10 ppm per century has been recently identified in older glacial periods, specifically during Marine Isotope

Author contributions: D.N., E.B., and C.B. designed research; K.A.W., C.N.-A., K.N., M.K., S.A.M., and C.B. performed research; K.A.W., C.N.-A., K.N., L.M., J.G., J.W.B.R., J.S., H.F., T.F.S., J.M., D.F., S.A.M., E.B., and C.B. analyzed data; and K.A.W., L.M., J.G., J.W.B.R., J.S., H.F., T.F.S., J.M., D.F., E.B., and C.B. wrote the paper.

The authors declare no competing interest.

This article is a PNAS Direct Submission.

[1]To whom correspondence may be addressed. Email: Kathleen.wendt@oregonstate.edu.

This article contains supporting information online at https://www.pnas.org/lookup/suppl/doi:10.1073/pnas.2319652121/-/DCSupplemental.

Published May 13, 2024.

Stages 10 and 12 (17). However, current records of CO_2 during the last glacial period are limited by >100-y resolution (21), and therefore lack the necessary detail needed to examine the exact timing, rate, and magnitude of these rapid carbon-cycle events associated with all HSs of the last glacial period.

The drivers and source of these centennial-scale CO_2 jumps are unknown. The proposed mechanisms include enhanced ocean–atmosphere CO_2 exchange in the Southern Ocean (via wind-driven upwelling of carbon-rich deep waters or invigorated convection), surface ocean temperature changes (impacting CO_2 solubility), biomass burning (via NH subtropical wildfires), or a combination of mechanisms (18, 23–29). The ongoing debate on CO_2 sourcing is exemplified by a lack of consensus in Earth system and ocean models, which disagree on the sign of change from terrestrial sources and the dominant oceanic source region when forced with idealized stadial conditions (30). Improving the characterization of CO_2 jumps during HSs is important for identifying the mechanisms by which abrupt shifts in atmospheric and oceanic circulation may alter carbon sources and sinks, with relevance to climate change in both the past and future.

Results

Our high-resolution WD CO_2 record reveals variations in atmospheric CO_2 levels that can be examined at comparable temporal resolution to atmospheric CH_4 variations and the oxygen and hydrogen isotopes of Antarctic ice (henceforth referred to as water isotopologs) across HSs 2 to 5 (Fig. 1). Abrupt rises in atmospheric CO_2 levels are clearly identifiable during HSs 1, 2, 4, and 5, with a smaller-magnitude jump during HS-3 that does not exceed background variability, yet has the same phasing relative to CH_4 and Antarctic water isotopologs as seen during other HSs (Fig. 2).

Each increase in CO_2 is resolved by multiple data points that were replicated by 2 to 3 measurements at each depth. No relationship between the timing of WD CO_2 variability and the carbonate dust in the ice is observed that would suggest in situ production of CO_2 (*SI Appendix*, Fig. S1). To test reproducibility, a WD replicate core spanning HS-4 was measured across 42 depths at the University of Bern using a friction-free dry-extraction technique (17, 31) (*Materials and Methods*). Absolute CO_2 values produced in the separate laboratories were reproducible to within an average of 1.6 ppm (*SI Appendix*, Fig. S2). This small offset is likely due to small differences in methods and/or standard materials used in the separate laboratories.

To determine the timing, duration, and magnitude of the rapid CO_2 jumps associated with HSs 2 to 5, we employed the function Rampfit (37). The largest Rampfit-determined feature is a 14.0 ± 0.8 ppm CO_2 increase within 55 ± 10 y starting at 39.5 ± 0.4 ka (2σ) during HS-4 (Fig. 2), with a full amplitude (peak-to-peak) of 18 ppm. The CO_2 rise observed during HS-4 is comparable in magnitude and duration to the CO_2 jump associated with HS-1, during which a Rampfit-determined jump of 12 ± 0.7 ppm over 75 ± 20 y is observed (18). The Rampfit-estimated rate of rise is 0.25 ppm/y during HS-4 and 0.16 ppm/y during HS-1. Lower magnitude jumps of 8 ± 1.4 ppm during HS-5 (48.4 ± 0.4 ka) and 4 ± 0.9 ppm during HS-3 (30.3 ± 0.3 ka) occurred within 150 ± 50 y and 125 ± 10 y, respectively. A rapid jump of 7 ± 1.2 ppm occurred within 15 ± 10 y during HS-2 (24.1 ± 0.3 ka). For HS-1, HS-3, and HS-4, higher CO_2 concentrations are maintained after the abrupt event, while for HS-2 and HS-5, the CO_2 jump is part of a short-lived excursion. These rates of CO_2 increase are among the most rapid seen in the ice core record, yet still about an order of magnitude slower than the current rate of anthropogenic CO_2 rise (38).

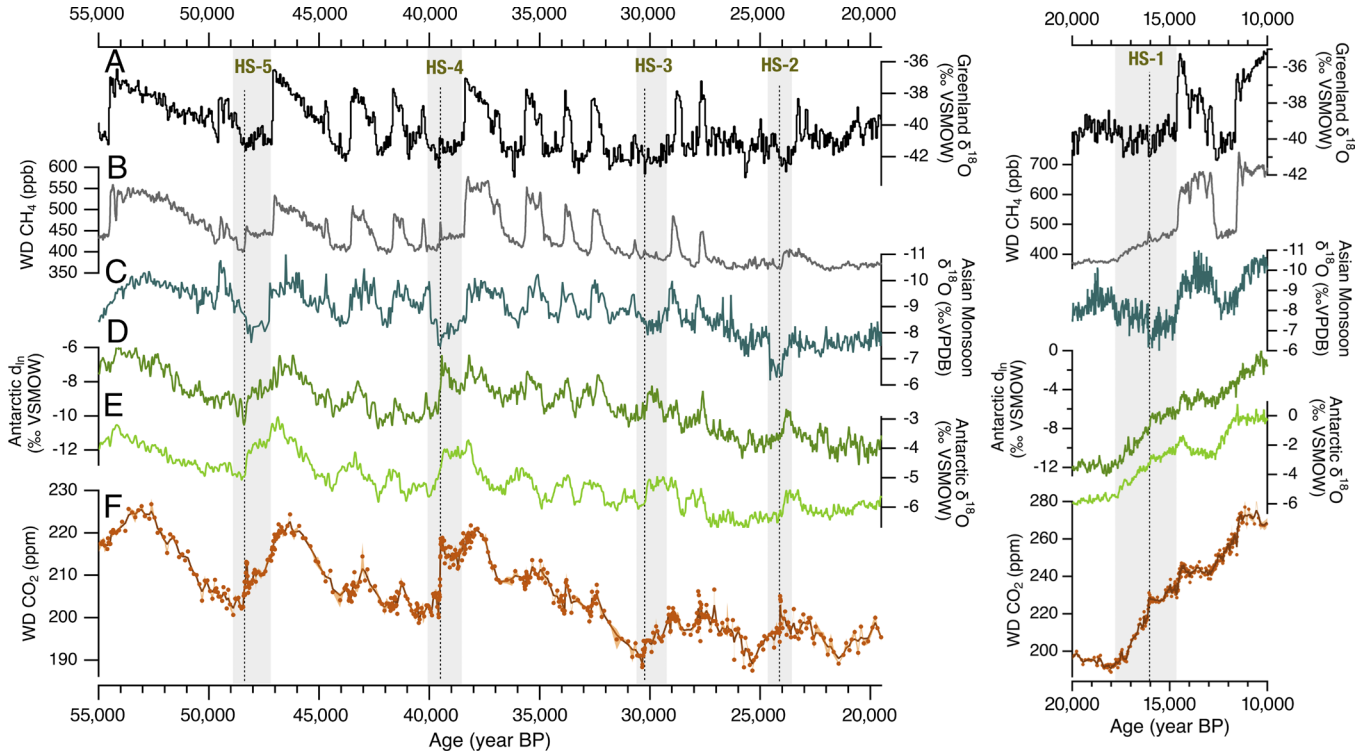

Fig. 1. Paleoclimate records of polar climate, greenhouse gas variability, and East Asian monsoon intensity reflecting meridional displacement of the Intertropical Convergence Zone. (*A*) Averaged $\delta^{18}O$ from Greenland Ice Core Project (GRIP) and Greenland Ice Sheet 2 (GISP2) (black) (32, 33) on the GICC05 timescale (34) multiplied by 1.0063 after 31 ka (35), (*B*) WAIS Divide (WD) CH_4 (gray) (15), (*C*) Chinese speleothem $\delta^{18}O$ (blue) (11), (*D*) Antarctic six-core average d_{ln} (dark green) (36), (*E*) Antarctic six-core average $\delta^{18}O_{ice}$ (light green) (36), (*F*) WD CO_2 (orange dots) with binomial smoothed average (dark orange line), and pooled 1σ standard uncertainty (orange shading) (this study; 18, 21). Gray bars show the timing of Heinrich Stadials (HS) 1 to 5 (*SI Appendix*, Table S1). Dashed lines represent timing of decadal- to centennial-scale rises and decreases in WD CO_2 and CH_4, respectively.

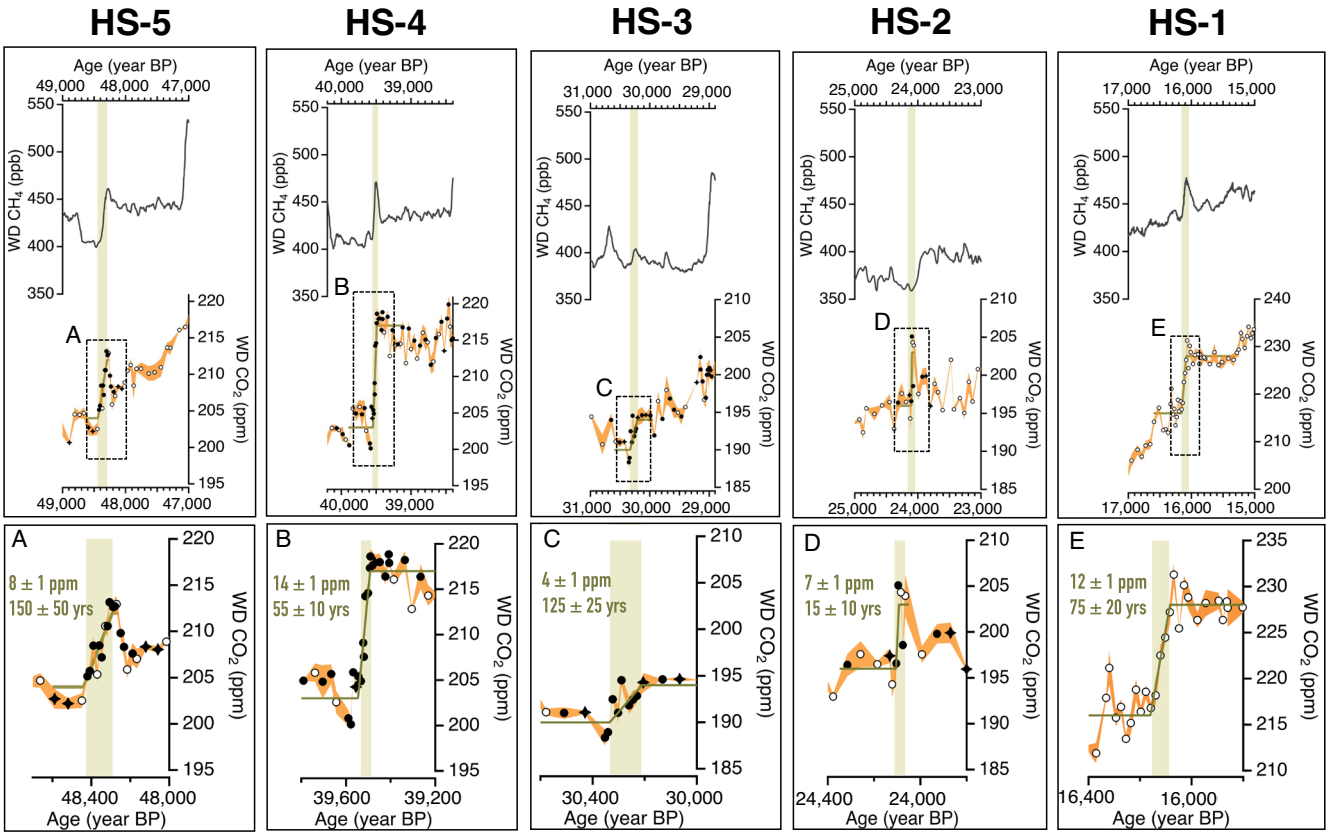

Fig. 2. Centennial-scale CO_2 and CH_4 variability during Heinrich Stadials 1 to 5. *Upper* panel: WD CH_4 (15), WD CO_2 from this study (closed circles), and previous publications (open circles) (18, 21) and replicated from previous publications (closed black diamonds). Light orange shading represents pooled 1σ standard uncertainty of individual CO_2 measurements. Shaded vertical bars highlight centennial-scale jumps in WD CO_2 and CH_4. Green lines indicate breakfit determinations (see text). *Lower* panel: WD CO_2 as in *Upper* panel sections *A*–*E*, with the magnitude and duration of abrupt CO_2 transitions shown in green.

Discussion

As with HS-1, the multi-decadal- to centennial-scale jumps in CO_2 associated with HSs 2 to 5 are synchronous with an abrupt, short-lived rise in atmospheric CH_4 concentrations recorded in the same ice core (15, 18) (Fig. 2). CH_4 changes during an HS are interpreted as follows: cooler NH temperatures prompted a southward shift of the ITCZ (13), resulting in drying of the NH tropics (10, 11) and a subsequent decrease in CH_4 emissions via a desiccation of NH wetlands (9, 15) and reduction in their carbon stock (39). High-resolution sampling of ice cores reveals a smaller-magnitude (10s ppb) multi-decadal-scale increase in CH_4 that occurs approximately midway through each HS (15, 18, 40). The timing of the mid-HS jump in atmospheric CH_4 levels associated with HS-1 (the HS with best age control) coincides with the onset of ice-rafted debris deposition in the North Atlantic, within age uncertainties (22). Rhodes et al. (15) argue that NH cold intervals associated with ice rafting events triggered a maximum southerly displacement of the ITCZ, as corroborated by subtropical rainfall proxy evidence (10, 11, 16), which led to an expansion of SH subtropical wetlands and a subsequent increase in CH_4 emissions. This rapid reorganization of global atmospheric circulation likely occurred within a decade of the initiation of ice rafting events (14); thus, mid-HS jumps in atmospheric CH_4 are interpreted as an indirect proxy for the timing of HEs (15).

Ice cores also reveal a 0.2 to 0.25‰ depletion in the carbon isotopic composition of CO_2 ($\delta^{13}C$–CO_2) that coincides with CO_2 and CH_4 jumps during HS-1 and HS-4 (20, 29) (Fig. 3). Similar high-resolution $\delta^{13}C$–CO_2 data are unavailable for the other events. $\delta^{13}C$–CO_2 reflects combined changes in the terrestrial carbon pool, marine export production, oceanic circulation, and air–sea gas exchange linked to temperatures (29, 41, 42). Explaining the multi-decadal- to centennial-scale jump in CO_2 during HSs requires a mechanism that is directly or indirectly linked to concurrent jumps in CH_4 and depletion of $\delta^{13}C$–CO_2.

Here, we examine the hypothesis that abrupt shifts in global atmospheric circulation facilitated concomitant rises in CH_4 and isotopically light CO_2 during HSs. General ocean–atmosphere circulation model simulations suggest that the SH westerlies respond in parallel to latitudinal shifts in the ITCZ (8, 46, 47), with a southward shift in the ITCZ prompting a poleward shift and strengthening of the SH westerlies. A poleward intensification the SH westerlies during HSs 1 to 6 and HS-11 is supported by increased salt leakage in the Agulhas Corridor (48–50), increased rainfall in western Patagonia during HS-1 (51), maximum opal productivity in the Southern Ocean during HSs 1 to 5 (24), and a poleward shift in the Southern Ocean SST front latitude (i.e., the latitude at which meridional SST gradient is steepest) during HS-1 (28). Numerical models suggest that poleward intensification of the SH westerlies enhances Southern Ocean ventilation and rapidly releases CO_2 from the ocean interior (26, 52–54). Even when taking into account the mesoscale response to the wind-driven circulation, increased SH westerly wind stress and parallel changes in surface buoyancy fluxes are thought to enhance the upwelling of deep and mid-depth, carbon-rich waters in the Antarctic Zone of the Southern Ocean (26, 53–56).

Enhanced Southern Ocean ventilation and Southern Ocean–atmosphere CO_2 exchange during HSs is supported by southern high-latitude sediment records (Fig. 3), which suggest enhanced Antarctic Bottom water formation that delivers cold water to depth

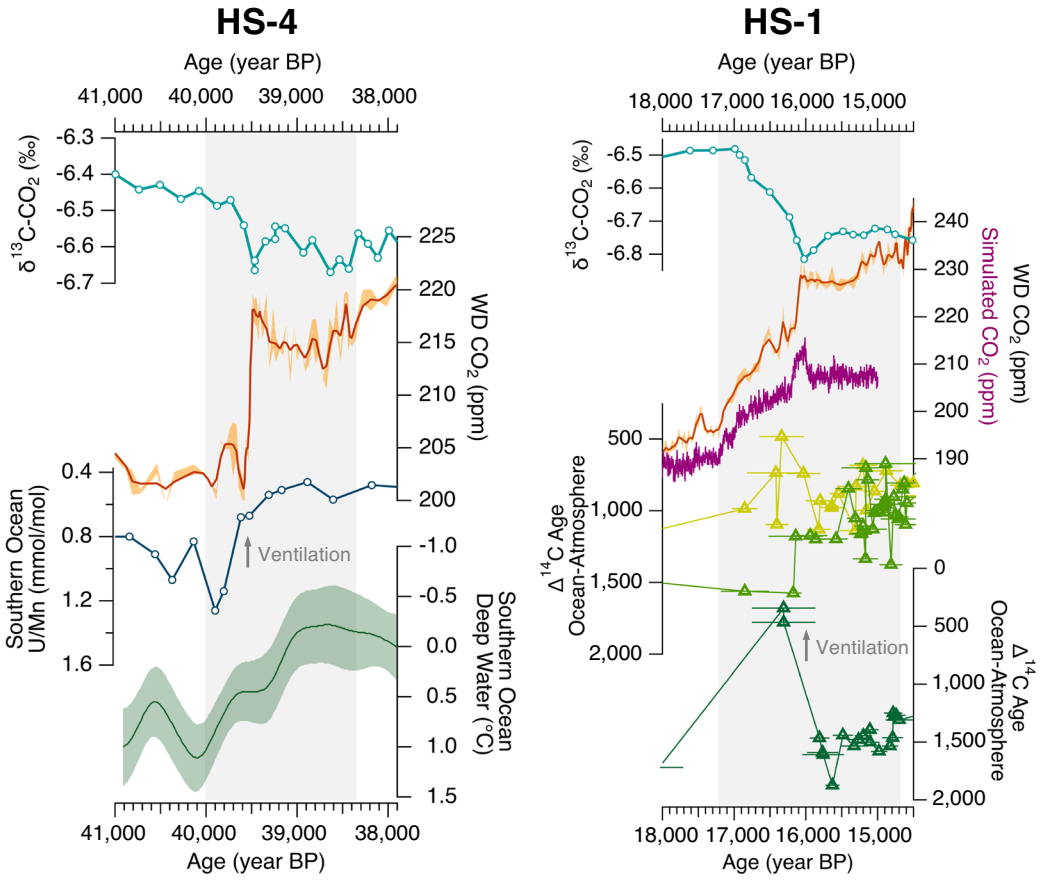

Fig. 3. Atmospheric δ ^{13}C–CO_2, CO_2, and Southern Ocean marine sediment proxies during HS-4 and HS-1. *Left* panel: Taylor Glacier δ^{13}C–CO_2 (light blue) (20), WD CO_2 (orange) (this study; 21), South Atlantic sediment proxies for deep-water oxygenation (blue) (43), and deep-water temperature (44). *Right* panel: δ^{13}C–CO_2 (light blue) (29), WD CO_2 (orange) (this study; 21), simulated atmospheric CO_2 (pink) (26;LH1-SO-SHW simulation), and difference in Southern Ocean and atmosphere ^{14}C ages from shallow (yellow), intermediate (green), and deep (dark green) corals (27, 45) including 2σ U-Th dating uncertainties. Respectively, 160 and 150 y were subtracted from the Taylor Glacier chronology to align Taylor Glacier and WD CO_2 peaks at HS4 and HS1.

(44), greater deep water oxygenation (43, 44), lower Southern Ocean ^{14}C ventilation ages (43, 45, 57–59), and increased upwelling (24). A depletion of atmospheric δ^{13}C–CO_2 (20, 29, 42) (Fig. 3) and enrichment of benthic foraminiferal δ^{13}C south of 30°S (58–61) during HSs are consistent with a wind-driven release of isotopically light carbon from ventilation of the ocean interior. ^{14}C-based ventilation reconstructions from precisely dated deep-sea corals also suggest deep vertical mixing in the Southern Ocean during HS-1 (27, 45, 62) (Fig. 3) with a distinct centennial-scale pulse of deep ocean ventilation around 16.3 ± 0.4 (2σ) ka (27) which is within the dating uncertainty of the rapid CO_2 rise in HS-1 recorded in the WD ice core (Fig. 3).

Previous studies show that enhanced vertical transport in the Southern Ocean during HSs would likely result in increased sea surface temperatures (SST) due to enhanced upwelling of relatively warm Circumpolar Deep Water (26, 44, 63, 64) (Fig. 3). Temperature reconstructions from precisely dated corals support this hypothesis, with an abrupt ~5 °C warming centered on the interval of rapid CO_2 rise within HS-1 in corals bathed by waters sourced from the Southern Ocean surface (65). However, resolving centennial-scale Southern Ocean SST anomalies beyond the coral record remains a challenge, given sediment mixing by benthic organisms, insufficient marine sedimentation rates, and poor calcite preservation. To circumnavigate these issues, we examine the relative phasing of high-resolution Antarctic water isotopolog records and abrupt atmospheric CO_2 jumps during HSs at multidecadal precision. Variations in oxygen isotopes (δ^{18}O) in the ice phase of ice cores largely reflect changes in site air temperatures. Deuterium excess (d_{ln}) is a second-order isotope parameter that reflects temperature conditions during source evaporation. Previous work shows that d_{ln} is positively correlated with SSTs at the vapor origin site (66), and it has been used to reconstruct source water temperatures (66–69). To examine similarities across all four HSs, we construct composite (or stacked) records of i) WD CO_2, ii) WD CH_4, iii) δ^{18}O, and iv) d_{ln} averaged from six Antarctic ice cores [EPICA Dome C (EDC), EPICA Dronning Maud Land (EDML), South Pole (SP), Talos Dome (TAL), Dome Fuji (DF), and WAIS DIVIDE (WD); Fig. 4]. We also compare the (v) site and (vi) vapor source temperatures calculated by Markle and Steig (67) using δ^{18}O and d_{ln} records from each ice core (Fig. 4). We interpret the stacked records as a faithful representation of an Antarctic-wide signal of continental surface temperatures and Southern Ocean-wide SSTs for all 5 HSs (Fig. 4).

Results show a jump in atmospheric CO_2 concentrations associated with HSs 1 to 5 that averages +9 ppm over a 100-y envelope surrounding the atmospheric CH_4 mid-point (CO_2 jumps an average of +12 ppm when stacking only HS-1, -4, -5). An abrupt 0.4‰ rise in δ^{18}O and 0.7‰ rise in d_{ln} occurred within the first century following the mid-point of each ~40 ppb jump in atmospheric CH_4 levels (Fig. 4), with both proxies reaching maximum values within two centuries after the onset of atmospheric CO_2 rise. On average, HSs show an abrupt 0.6 °C rise in site temperatures and 0.4 °C rise in vapor-source temperatures within the first century following the mid-point of each CH_4 jump, reaching maximum values of approximately 1.3 °C and 0.6 °C, respectively, within the second century (67). Overall, the data suggest an abrupt centennial-scale increase in Southern Ocean SSTs associated with

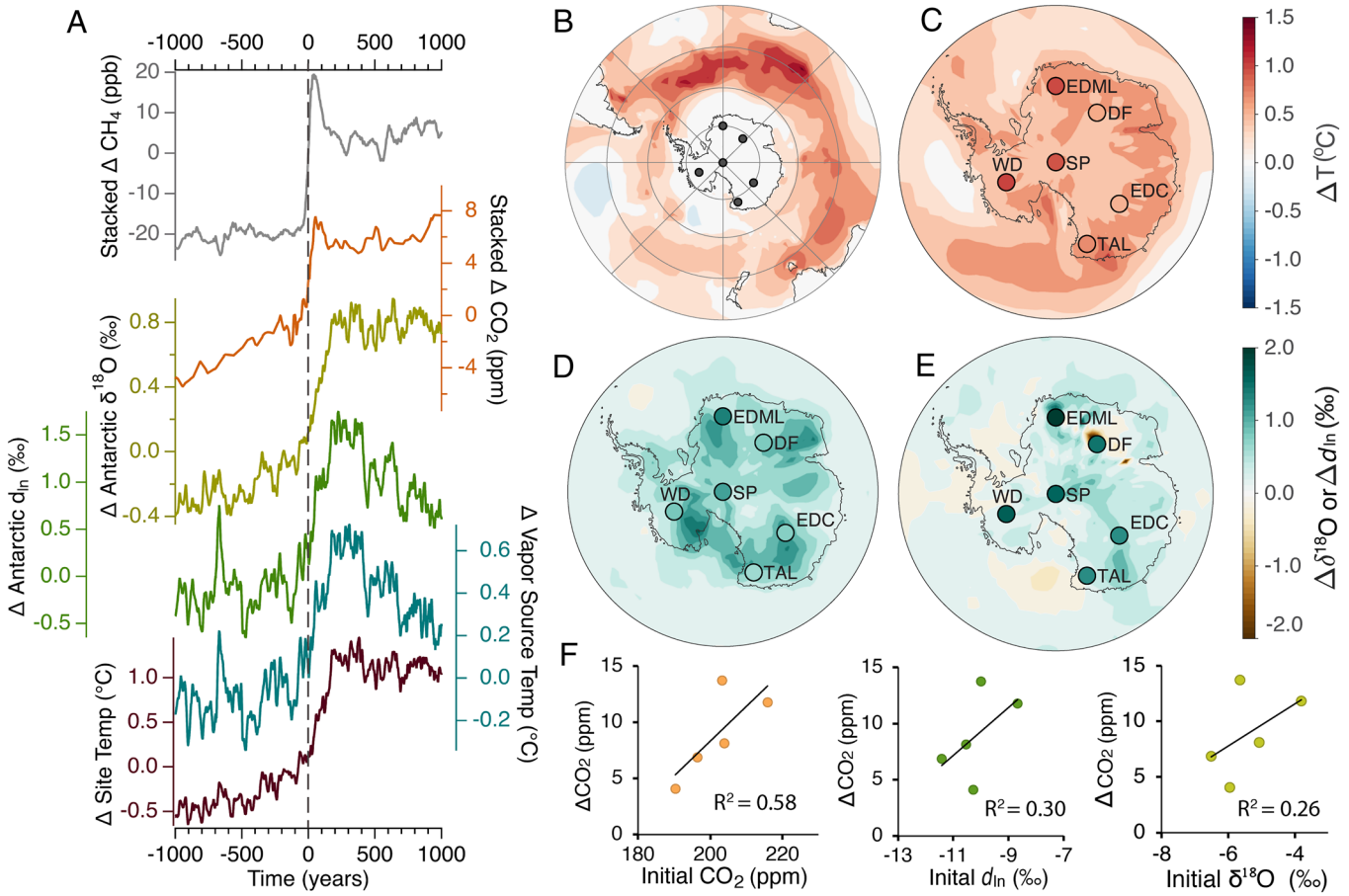

Fig. 4. Centennial-scale Antarctic temperature response during Heinrich Stadials. (*A*) Stacked average change in WD CH_4 (gray) (15), WD CO_2 (orange) (this study), Antarctic $\delta^{18}O$ (yellow) (36), Antarctic d_{ln} (green) (36), vapor source temperature (blue) (67), and site temperature (purple) (67) during HSs 1 to 5. Time "0" represents the mid-point of the associated WD CH_4 jump in HSs 1 to 5 (see text). (*B*) SST anomaly forcing based on Ferreira et al. (64) in response to a poleward displacement of the SH westerlies. The SST response from Ferreira et al. (64) was multiplied by two to better match Antarctic water isotopologs. Spatial pattern of the differences in (*C*) modeled surface temperature, (*D*) $\delta^{18}O$ (*D*), and (*E*) d_{ln} simulated in iCAM5 before and after imposing SST temperature forcing as shown in (*B*). Location, abbreviation, and HSs proxy value of each ice core are indicated on each map by the colored dots. (*F*) Scatter plots showing the magnitude of change in WD CO_2 concentrations and HSs proxies associated with HSs 1 to 5 versus background values for CO_2, d_{ln}, and $\delta^{18}O$).

a mid-HS increase in atmospheric CH_4 and CO_2 concentrations. Alternative interpretations of the d_{ln} signal include a northward shift of the vapor source and thus an apparent warming in water isotopologs, however, this would fail to account for the observed site warming. The increase in greenhouse radiative forcing from each CO_2 jump (e.g., 0.35 W/m^2 at HS-4) accounts for ≤20% of the ~1 °C change in SSTs as indicated by our stacked Antarctic $\delta^{18}O$ record and is therefore insufficient to explain the full magnitude of SST increase (*Materials and Methods*). Instead, the upwelling of warm, CO_2-rich water masses accounts for both a release of heat and $\delta^{13}C$-depleted CO_2 from the Southern Ocean to the atmosphere (42, 44) (Fig. 3).

To assess whether a multi-decadal-scale increase in Southern Ocean SST due to wind-driven upwelling could influence Antarctic ice core $\delta^{18}O$ and d_{ln}, we perform a series of experiments using the isotope-enabled Community Atmosphere Model 5 (iCAM5) (70). To apply an SST anomaly between 45°S and 60°S (approximate latitudinal band of SH westerlies) that broadly matches the 0.4 °C warming implied by ice core d_{ln}, we multiplied the SST anomaly from Ferreira et al. (64) by a factor of 2 (*Materials and Methods*) and applied this SST anomaly to the iCAM5 model under LGM background climate conditions (Fig. 4*B* and *SI Appendix*, Table S3). The simulated anomalies in surface air temperature, precipitation $\delta^{18}O$, and precipitation d_{ln} (Fig. 4 *C*–*E*) are compared to the abrupt HS signals reconstructed from the Antarctic ice cores (Fig. 4 *C*–*E*). We find that the model correctly captures the sign of all three signals, yet underestimates the magnitude of the d_{ln} shift (*SI Appendix*, Table S3). Similar results are obtained using the simulated SST anomaly from a transient experiment of HS-1 with stronger SH westerlies (LH1-SHW in ref. 26; *SI Appendix*, Fig. S4) as well as an idealized 1 °C SST warming anomaly (*SI Appendix*, Fig. S5), suggesting that the spatial details of the warming pattern are of secondary importance in explaining the magnitude of the observed d_{ln} shift. In addition, model results predict continent-wide increases in Antarctic snow accumulation rates in parallel with the isotope changes to SST anomalies (*SI Appendix*, Fig. S7). Overall, the iCAM5 simulations support the hypothesis that the observed increase in Antarctic $\delta^{18}O$ and d_{ln} can be explained by a rise in Southern Ocean SST, which is anticipated to occur during intervals of increased wind-driven upwelling due to a poleward intensification of the SH westerlies.

The magnitude of change in Antarctic water isotopologs is consistent between HSs 1 to 5 (Fig. 4*F* and *SI Appendix*, Fig. S8), even for those HSs that show little to no changes in AMOC such as HS-2 and HS-3 (71). By contrast, the magnitude of the abrupt jumps in atmospheric CO_2 levels that occur mid-HS is variable among HSs 1 to 5 and ranges from 4 ± 1 ppm during HS-3 to 14 ± 1 ppm during HS4. We find that the magnitude of rapid atmospheric CO_2 jumps is correlated with background climate conditions, defined here as the temperature proxy values ($\delta^{18}O$ and d_{ln}) prior to each event, such that colder climate states (lower atmospheric CO_2, $\delta^{18}O$ and d_{ln}) tend to have a smaller mid-HS CO_2 jump (Fig. 4*F* and *SI Appendix*, Fig. S8). We speculate that

background climate may control the extent of Antarctic sea ice, which in turn may control the extent of ocean–atmosphere CO_2 exchange (72, 73).

High-resolution isotopic data from Antarctic ice support the hypothesis that SH high-latitude changes are different for Heinrich and non-Heinrich stadial phases of the Dansgaard–Oeschger (DO) cycle (74) and that the former is not simply an amplified version of the latter. While gradual Antarctic warming via the thermal bipolar seesaw occurs during all DO stadials (Heinrich and non-Heinrich alike), our results suggest that abrupt Southern Ocean SST warming occurs during HSs only, whereas no such abrupt Southern Ocean SST warming is seen during non-HS DO stadials (36). Similarly, no abrupt rises in atmospheric CO_2 or CH_4 are observed during non-HS DO stadials (15, 21). This qualitative difference may reflect a nonlinear (threshold) response in the strength or zonal pattern of the SH westerlies during North Atlantic stadial periods, or perhaps the strong involvement of the AMOC and/or Pacific Ocean in HE dynamics (6, 75, 76).

Our decadal-resolution atmospheric CO_2 record from the WD ice core reveals multi-decadal- to centennial-scale jumps in atmospheric CO_2 levels that are synchronous with jumps in atmospheric CH_4 concentrations and Antarctic water isotopologs during HSs (15, 36). The synchroneity of these jumps can be explained by a southward displacement of the ITCZ in response to North Atlantic ice rafting events, which ultimately led to a poleward enhancement of the SH westerlies. Enhanced wind stress drove increased vertical transport and ventilation of deep waters in the Southern Ocean, resulting in rapid CO_2 outgassing that drove a pulse of atmospheric CO_2 rise of up to 14 ppm within half a century. Other potential mechanisms, including a multidecadal scale release of CO_2 from a terrestrial carbon pool, cannot be excluded and may have occurred in parallel to Southern Ocean changes. The rate and magnitude of atmospheric CO_2 rises resolved in this study provide critical constraints on carbon-cycle variability during abrupt climate shifts and urge caution that the modern-day Southern Ocean carbon sink has the potential to weaken in response to continued poleward enhancement of the SH westerlies (28, 77).

Materials and Methods

A total of 453 measurements were made from 249 individual depth levels on the WAIS Divide Ice core (79.48°S, 112.11°W). Measurements spanning HSs 2 to 5 have a median sampling resolution of 25 y (*SI Appendix*, Table S1). The timing of HSs 2 to 5 is defined in Martin et al. (74). The mean pooled 1σ SD of all measurements is 0.7 ppm.

CO_2 amount fractions were determined using dry extraction methods at Oregon State University, Corvallis, USA (78). Subsamples were cut at 0.5 to 0.15 m intervals along selected depths of the WD ice core using a Laguna bandsaw in a −25 °C walk-in freezer. Bandsaw blade and tabletop surface were decontaminated with ultrapure ethanol. On the morning of extraction, subsamples were trimmed into ~2.5 cm wide cubes with an average mass of 12 ± 1 (1σ) g.

Subsamples were inserted into a custom-designed stainless-steel vacuum chamber cooled to −35 °C then crushed 50 times using a stainless-steel plate containing 91 steel pins. The liberated air was expanded to a stainless-steel coil water trap in an ethanol dewar flask cooled to −85 °C, and then condensed in a 6 cm^3 stainless-steel sample tube housed in a cryogenic system at 10 K. Total extraction time per sample was 7 min. Following extraction, sample tubes were warmed to room temperature using a water bath. The air (~1 cm^3 at standard temperature and pressure) was then expanded into an Agilent 6890 N Gas Chromatograph using a vacuum inlet line connected to a sample loop (5 cm^3) installed on a six-port two-position VICI Valco valve. Pressures in the sample loop were measured with a high-precision MKS 622 Baratron capacitance manometer (0.15% accuracy). The GC system is fitted with a Ni catalyst and flame-ionization detector. N_2 was used as the carrier gas to maximize the detector stability over a greater range of air-flow rate and temperature conditions. Signals were acquired and integrated using Agilent ChemStation software.

The extracted ice core air was calibrated to dry standard air from the National Oceanic and Atmospheric Administration (NOAA) Earth System Research Laboratory with a known amount fraction of 268.80 ± 0.01 ppm on the WMOX2019 scale for reference gases. In-house verification of standard air values using a lower concentration standard (197.54 ± 0.03 ppm on WMOX2019 scale) yielded no difference between the assigned and measured values within uncertainties. CO_2 amount fractions measured prior to 2019 that were originally calibrated to WMOX2007 are presented here on the updated to the WMOX2019 scale (difference in calibrated results is <0.02 ppm). The amount fractions of standards used here represent the range expected for atmospheric CO_2 concentrations during the last glacial (21). Daily calibrations were performed by introducing standard air to the sample loop at a pressure range comparable to the sample air aliquots. Typical precision for standard air is ~0.2 ppm (1σ) for n = 6 measurements. A daily calibration curve was constructed using a second-order polynomial fit, as outlined in ref. 78.

Two additional variables were monitored during sample extraction and analysis: i) instrumental drift and ii) adsorption or desorption of CO_2 on the surface of the vacuum chamber during extraction. Instrumental drift includes both variations in baseline (i.e., GC sensitivity) and slope of the calibration curve. The former is automatically detected and subtracted by Agilent ChemStation software, while the latter is monitored daily by bracketing sample measurements with standard air analyses. Measured standard air values, as determined by respective calibration slopes before and after sample measurements, showed no difference within uncertainties. Potential adsorption or desorption of CO_2 was monitored by introducing standard air into the system following crushing. The expanded standard air was then collected in a separate sample tube following normal sampling procedures. Each measurement for a crushed sample is corrected by adding or subtracting the detected net offset from the calibrated standard value. Mean offsets were 4 ± 3.8 (1σ) ppm throughout sampling.

To determine background values, standard air was expanded over air-free ice and measured using standard methods (78). Gas-free ice was made by boiling deionized water in a vacuum chamber, and then slowly freezing it by placing the chamber in an ethanol bath. One standard air-over-gas-free-blank-ice measurement was performed every 10th sample measurement in order to quantify the influence of the extraction procedure on the raw measurement results. Measurement of gas-free ice resulted in a 0.96 ± 1.02 (1σ) ppm CO_2 enrichment of standard air (n = 61 measurements over 2 y). The detected ratio of CO_2 enrichment per mass of gas-free ice was used to determine the total contamination per sample mass, which was subtracted from results. Averaged biweekly background values averaged 0.3 ppm/g and ranged from 0.6 to 0.1 ppm/g ice. Raw CO_2 amount fractions were additionally corrected for gravitational enrichment using $\delta^{15}N\text{-}N_2$ from ref. 79, with gravitational effects ranging from 1.0 to 1.4 ppm. Each sampling depth was replicated 2 to 3 times.

Gas ages were interpolated from the WD2014 chronology (35, 80), which is synchronized to the radiometrically dated Hulu Cave record prior to ~30 thousand years BP (ka). The difference in age between the gas and ice phases (Δage) is relatively well constrained in WD (e.g., Δage uncertainties of ±73 y at 40 ka BP), such that the time of changes in CO_2 relative to the chemical composition of ice can be precisely determined.

Breakpoint Determination. To provide an objective means for determining the timing and duration of the CO_2 transitions across HSs, we employed the function Rampfit (37). Both the timing and duration of abrupt jumps in CO_2 were determined using 25 to 10-y time spacing. Calculated uncertainties are the result of 1,000 Monte Carlo analyses (*SI Appendix*, Table S2).

Record Stacking. We constructed a composite (or stacked) records for HSs recorded in WD CO_2, WD CH_4, and water isotopologs from six ice cores across Antarctica [EPICA Dome C (EDC), EPICA Dronning Maud Land (EDML), South Pole (SP), Talos (TAL), Dome Fuji (DF), and WAIS DIVIDE (WD)]. Individual HSs were aligned and then averaged to identify their common climatic signal. The methods described here are identical to stacking methods used in ref. 35. We define the midpoint ($t = 0$) of the abrupt CH_4 transitions associated with HSs 1, 2, 4, and 5. We excluded HS-3 due to its relatively low signal. We define a time vector τ that runs from time $t = -1{,}200$ to $t = 1{,}200$ in 1-y increments. The WD06 CO_2

and CH_4 records were resampled at annual time steps onto time vector τ. The uniformly sampled events were averaged to obtain the stacked record. The same methods were used to stack site and source temperature reconstructions (67) from the same six ice cores, as well as $\delta^{18}O$ and d_{ln} in the logarithmic definition from each respective ice core.

External Reproducibility. The WD replicate core (WDC-R1) was measured at Climate and Environmental Physics (CEP), Physics Institute, University of Bern, Switzerland, using the Centrifugal Ice Microtome (CIM) in 2017. Using this friction-free dry-extraction method, we performed a total of 132 single measurements on 42 depth levels with three true replicate measurements for each depth level (*SI Appendix*, Fig. S2). In four cases, four to five single measurements of two directly vertically adjacent samples (2 cm apart) were averaged and are reported as a single value for their average depth. At least 3 to 5 mm were trimmed from all outer surfaces that were in contact to the atmosphere prior to sampling. The average sample weight was 7.74 ± 0.30 g (1σ). The pooled SD of 0.54 ppm for all depth levels is surprisingly low, probably owing to the high quality of the ice samples (little to no cracks or clathrate-relaxation features) and the number of true replicate measurements. One standard-air-over-gas-free-blank-ice measurement was performed for every four WD-R1 sample measurements to quantify the influence of the extraction procedure on the raw measurement results. The average correction for the extraction offset amounts to 1.85 ± 0.67 ppm (1σ). All measured raw CO_2 amount fractions have been corrected for gravitational enrichment using $\delta^{15}N$–N_2 from ref. 79. The average correction for this gravitational effect amounts to 1.24 ± 0.04 ppm (1σ). For a detailed description of the CIM method please refer to refs. 31 and 17. All Bern CO_2 measurements made using the CIM were originally referenced to the WMOX2007 amount fraction scale using four primary dry air standards calibrated at the NOAA Earth System Research Laboratory, Boulder, USA ranging between 192.44 ± 0.11 and 363.08 ± 0.06 ppm (17) and later transferred the WMOX2019 amount fraction scale (Dataset S1). Replicate core depths were corrected to align with main core (WD) depths using electrical conductivity data (81). At these depths, the average depth offset between WD-R1 and WD cores is 0.735 m (81).

Radiative Forcing Calculation. Changes in radiative forcing due to a rise of CO_2 concentrations were calculated using established equations (82). Assuming all other forcings are held constant, we can approximate the associated change in temperature using a simplified climate sensitivity equation:

$$\Delta T = F / \lambda,$$

where ΔT is the temperature change in response to the radiative CO_2 forcing (F), and λ is the climate feedback parameter ($Wm^{-2}K^{-1}$). λ can be approximated using the mean climate sensitivity per doubling of CO_2 (~3.25 °C) from the range of climate sensitivity estimates cited in recent literature (e.g., ref. 83).

Isotope-Enabled Modeling. In this study, we use an atmosphere-only modeling setup that is part of the Community Earth System Model 1.2 (CESM 1.2) (84). Specifically, we use the isotope-enabled Community Atmosphere Model (iCAM 5) (70). We use a nominal 2-degree finite volume resolution, with 96 × 144 latitude by longitude grid size, and 30 vertical levels. Precipitation isotope results from iCESM are well-verified (85).

For all model results presented here, the atmosphere-only iCAM5 model was run for 200 y. The first 50 y are treated as the model spin-up and removed, and the last 150 y were averaged to obtain the equilibrium monthly climatology. Rather than attempting to simulate the warming events dynamically, we instead run one equilibrium snapshot before and one after the abrupt event and interpret the difference between the two as the event magnitude. For the control (CTRL), we run iCAM5 using LGM background conditions (orbital configuration, atmospheric greenhouse gas concentrations, sea level, ice sheet topography), with land and sea surface conditions [including SST and sea ice coverage (SIC)] taken from fully coupled LGM atmosphere–ocean GCM simulations using the Community Climate System Model 4.

iCAM5 deuterium excess in Antarctica. The traditional linear definition of deuterium excess ($d = \delta^2H - 8 \times \delta^{18}O$) is not suitable for situations of strong isotopic depletion (e.g., interior Antarctica or the glacial period) where the δ^2H–$\delta^{18}O$ slope for equilibrium fractionation begins to deviate from the value of 8. Using the linear definition in such cases results in spurious signals in d that reflect equilibrium fractionation processes en route, rather than the kinetic fractionation at the vapor source regions that deuterium excess seeks to capture. To resolve this issue, Uemura et al. (86) introduced an empirical logarithmic definition of deuterium excess that more closely follows water-stable isotope fractionation systematics:

$$d_{ln} = \ln\left[1+\delta^2H\right] - \left(-2.85\times10^{-2}\times\left(\ln\left[1+\delta^{18}O\right]\right)^2 + 8.47\times\ln\left[1+\delta^{18}O\right]\right). \quad [1]$$

The Uemura d_{ln} definition is derived by performing a second-order polynomial fit between $\ln(1+\delta^{18}O)$ and $\ln(1+\delta^2H)$ in isotopic data from global meteoric waters and Antarctic snow, thereby ensuring that there is no residual trend between d_{ln} and $\delta^{18}O$ (86). Unlike the linear definition, the logarithmic definition of deuterium excess shows great coherence across Antarctica on orbital and millennial timescales making it more suitable for climatic interpretation (86–88).

The iCAM5 relationship between $\ln(1+\delta^{18}O)$ and $\ln(1+\delta^2H)$ in Antarctica for the LGM control run deviates slightly from the observational relationship (*SI Appendix*, Fig. S3). Therefore, Eq. **1** is not adequate when evaluating d_{ln} in these simulations. Following the approach by Uemura et al. (86), we perform a second order polynomial fit between the simulated $\ln(1+\delta^{18}O)$ and $\ln(1+\delta^2H)$ south of 45°S in the iCAM5 LGM control run (*SI Appendix*, Fig. S3) and derive the following operational definition of d_{ln} for iCAM5 LGM simulations:

$$d_{ln} = \ln\left[1+\delta^2H\right] - \left(-1.497\times10^{-2}\times\left(\ln\left[1+\delta^{18}O\right]\right)^2 + 9.058\times\ln\left[1+\delta^{18}O\right]\right). \quad [2]$$

We use Eq. **2** in our analysis of Antarctic d_{ln} in this paper. However, we urge caution in interpreting the d_{ln} results due to the observed model-data offset in the δ^2H–$\delta^{18}O$ relationship over Antarctica (*SI Appendix*, Fig. S3).

Southern Ocean SST anomalies. From studies that prescribe a forced and persistent shift in the SH westerlies, we expect a Southern Ocean SST warming on longer (decadal to centennial) timescales (26, 89), which is also the signal implied by the ice core isotopic signals (Fig. 4). To investigate the impact of such SST anomalies on water isotope ratios in Antarctic precipitation, we run a series of iCAM5 scenarios. We test three different Southern Ocean SST anomalies. First, we use the long-term (years 11 to 20) SST response to a southward shift in the SH westerlies (positive SAM anomaly) from the CCSM3.5 model as found in Ferreira et al. (64). The Ferreira et al. (64) SST anomaly was added to the monthly LGM CTRL climatology and used to force the atmospheric model. A better $\delta^{18}O$ model–data agreement was obtained after doubling the Ferreira et al. SST (64) anomaly, and that run is reported here. Second, we use the SST response from Menviel et al. (26) to a simulated southward shift around 16.3 ka BP in the SH westerlies in the LOVECLIM Earth system model run LH1-SHW (*SI Appendix*, Fig. S4). SST changes from Menviel et al. (26) are much stronger than those from Ferreira et al. (64)–even after multiplying the latter by a factor of 2. Third, we use an idealized SST anomaly that consists of a 1 °C SST warming in a 15 degrees wide latitudinal band (*SI Appendix*, Fig. S5), the southern edge of which is placed just north of the winter sea ice edge (to avoid applying any warming underneath the sea ice). This SST anomaly is added to the monthly LGM CTRL climatology. The three SST anomalies are shown in Fig. 4 and *SI Appendix*, Figs. S4 and S5, together with the simulated changes in surface air temperature (SAT), $\delta^{18}O$ of precipitation, and d_{ln} of precipitation. Root mean squared deviation of model results from proxy observations presented in *SI Appendix*, Table S3. See *SI Appendix* for additional discussion of modeling results.

Data, Materials, and Software Availability. All study data are included in the supporting information.

ACKNOWLEDGMENTS. We thank our editor and two anonymous reviewers for their helpful feedback leading to the improvement of this paper. This work was funded by the US NSF grants 1906143 (to C.B. and E.B.) and 1804133 (to C.B.). K.A.W. gratefully acknowledges the support from the Heising–Simons Foundation. H.F. and T.F.S. gratefully acknowledge the long-term support of ice core sciences at the University of Bern by the Swiss NSF (SNSF). We thank OSU undergraduates I. Lopez, S. Smith, E. Rebarchik, and M. Zadlo for assistance in the laboratory. We are grateful to B. Seth and J. Lee for their assistance with sample preparation at the University of Bern. Special thanks to T. Bauska for scientific input. We appreciate the support of the WAIS Divide Science

Coordination Office at the Desert Research Institute (DRI) of Reno, Nevada, and the University of New Hampshire for the collection and distribution of the WAIS Divide ice core and related tasks (NSF grants 1806133, 0230396, 0440817, 0944348, and 0944266). Additional support for this research came from the NSF Office of Polar Programs through their support of the Ice Drilling Program Office and the Ice Drilling Design and Operations group; the US National Ice Core Laboratory, for curation of the core; and the 109th New York Air National Guard for airlift in Antarctica.

Author affiliations: [a]College of Earth, Ocean, and Atmospheric Sciences, Oregon State University, Corvallis, OR 97330; [b]Climate and Environmental Physics and Oeschger Center for Climate Change Research, University of Bern, Bern CH-3012, Switzerland; [c]Atmospheric Environmental Science Department, National Physical Laboratory, London TW11 0LW, United Kingdom; [d]Climate Change Research Centre, Australian Centre for Excellence in Antarctic Science, University of New South Wales, Sydney NSW 2052, Australia; [e]Institute of Geosciences, Kiel University, Kiel 24118, Germany; [f]School of Earth and Environmental Sciences, University of St Andrews, St Andrews KY16 9TS, United Kingdom; [g]Centro Para el Estudio de Sistemas Marinos, El Centro Nacional Patagónico-Conicet, Puerto Madryn U9120ACD, Argentina; [h]Meteorology Department, University of Reading, Reading RG6 6ET, United Kingdom; and [i]Department of Geoscience, University of Wisconsin-Madison, Madison, WI 53706

1. G. Bond *et al.*, Evidence for massive discharges of icebergs into the North Atlantic ocean during the last glacial period. *Nature* **360**, 245–249 (1992).
2. H. Heinrich, Origin and consequences of cyclic ice rafting in the northeast Atlantic Ocean during the past 130,000 years. *Q. Res.* **29**, 142–152 (1988).
3. S. R. Hemming, Heinrich events: Massive late Pleistocene detritus layers of the North Atlantic and their global climate imprint. *Rev. Geophys.* **42**, RG1005 (2004).
4. A. H. Voelker, Global distribution of centennial-scale records for marine isotope stage (MIS) 3: A database. *Q. Sci. Rev.* **21**, 1185–1212 (2002).
5. L. Henry *et al.*, North Atlantic ocean circulation and abrupt climate change during the last glaciation. *Science* **353**, 470–474 (2016).
6. J. Lynch-Stieglitz, The Atlantic meridional overturning circulation and abrupt climate change. *Ann. Rev. Marine Sci.* **9**, 83–104 (2017).
7. T. F. Stocker, S. J. Johnsen, A minimum thermodynamic model for the bipolar seesaw. *Paleoceanography* **18**, 1087 (2003).
8. J. B. Pedro *et al.*, Beyond the bipolar seesaw: Toward a process understanding of interhemispheric coupling. *Q. Sci. Rev.* **192**, 27–46 (2018).
9. T. Blunier *et al.*, Asynchrony of Antarctic and Greenland climate change during the last glacial period. *Nature* **394**, 739–743 (1998).
10. G. Deplazes *et al.*, Links between tropical rainfall and North Atlantic climate during the last glacial period. *Nat. Geosci.* **6**, 213–217 (2013).
11. H. Cheng *et al.*, The Asian monsoon over the past 640,000 years and ice age terminations. *Nature* **534**, 640–646 (2016).
12. X. Wang *et al.*, Wet periods in northeastern Brazil over the past 210 kyr linked to distant climate anomalies. *Nature* **432**, 740–743 (2004).
13. A. J. Broccoli, K. A. Dahl, R. J. Stouffer, Response of the ITCZ to Northern Hemisphere cooling. *Geophys. Res. Lett.* **33**, L01702 (2006).
14. J. C. H. Chiang, C. M. Bitz, Influence of high latitude ice cover on the marine Intertropical Convergence Zone. *Clim. Dyn.* **25**, 477–496 (2005).
15. R. H. Rhodes *et al.*, Enhanced tropical methane production in response to iceberg discharge in the North Atlantic. *Science* **348**, 1016–1019 (2015).
16. K. A. Wendt *et al.*, Three-phased Heinrich Stadial 4 recorded in NE Brazil stalagmites. *Earth Planet. Sci. Lett.* **510**, 94–102 (2019).
17. C. Nehrbass-Ahles *et al.*, Abrupt CO_2 release to the atmosphere under glacial and early interglacial climate conditions. *Science* **369**, 1000–1005 (2020).
18. S. A. Marcott *et al.*, Centennial-scale changes in the global carbon cycle during the last deglaciation. *Nature* **514**, 616–619 (2014).
19. J. Ahn, E. J. Brook, A. Schmittner, K. Kreutz, Abrupt change in atmospheric CO_2 during the last ice age. *Geophys. Res. Lett.* **39**, L18711 (2012).
20. T. K. Bauska *et al.*, Controls on millennial-scale atmospheric CO_2 variability during the last glacial period. *Geophys. Res. Lett.* **45**, 7731–7740 (2018).
21. T. K. Bauska, S. A. Marcott, E. J. Brook, Abrupt changes in the global carbon cycle during the last glacial period. *Nat. Geosci.* **14**, 91–96 (2021).
22. D. A. Hodell *et al.*, Anatomy of Heinrich Layer 1 and its role in the last deglaciation. *Paleoceanography* **32**, 284–303 (2017).
23. J. R. Toggweiler, J. L. Russell, S. R. Carson, Midlatitude westerlies, atmospheric CO_2, and climate change during the ice ages. *Paleoceanography* **21**, PA2005 (2006).
24. R. Anderson *et al.*, Wind-driven upwelling in the Southern Ocean and the deglacial rise in atmospheric CO_2. *Science* **323**, 1443–1448 (2009).
25. H. Fischer *et al.*, The role of Southern Ocean processes in orbital and millennial CO_2 variations–A synthesis. *Q. Sci. Rev.* **29**, 193–205 (2010).
26. L. Menviel *et al.*, Southern Hemisphere westerlies as a driver of the early deglacial atmospheric CO_2 rise. *Nat. Commun.* **9**, 2503 (2018).
27. T. Li *et al.*, Rapid shifts in circulation and biogeochemistry of the Southern Ocean during deglacial carbon cycle events. *Sci. Adv.* **6**, eabb3807 (2020).
28. W. R. Gray *et al.*, Poleward shift in the Southern Hemisphere westerly winds synchronous with the deglacial rise in CO_2. *Paleoceanogr. Paleoclimatol.* **38**, e2023PA004666 (2023).
29. T. K. Bauska *et al.*, Carbon isotopes characterize rapid changes in atmospheric carbon dioxide during the last deglaciation. *Proc. Natl. Acad. Sci. U.S.A.* **113**, 3465–3470 (2016).
30. J. Gottschalk *et al.*, Mechanisms of millennial-scale atmospheric CO_2 change in numerical model simulations. *Q. Sci. Rev.* **220**, 30–74 (2019).
31. B. Bereiter, T. Stocker, H. Fischer, A centrifugal ice microtome for measurements of atmospheric CO_2 on air trapped in polar ice cores. *Atmos. Meas. Tech.* **6**, 251–262 (2013).
32. S. J. Johnsen *et al.*, The δ18O record along the Greenland Ice Core Project deep ice core and the problem of possible Eemian climatic instability. *J. Geophys. Res. Oceans* **102**, 26397–26410 (1997).
33. M. Stuiver, P. M. Grootes, GISP2 oxygen isotope ratios. *Q. Res.* **53**, 277–284 (2000).
34. A. Svensson *et al.*, A 60 000 year Greenland stratigraphic ice core chronology. *Clim. Past* **4**, 47–57 (2008).
35. C. Buizert *et al.*, The WAIS Divide deep ice core WD2014 chronology–Part 1: Methane synchronization (68–31 ka BP) and the gas age–ice age difference. *Clim. Past* **11**, 153–173 (2015).
36. C. Buizert *et al.*, Abrupt ice-age shifts in southern westerly winds and Antarctic climate forced from the north. *Nature* **563**, 681–685 (2018).
37. M. Mudelsee, Ramp function regression: A tool for quantifying climate transitions. *Comput. Geosci.* **26**, 293–307 (2000).
38. V. Masson-Delmotte *et al.*, "Climate change 2021: The physical science basis" in *Contribution of Working Group I to the Sixth Assessment Report of the Intergovernmental Panel on Climate Change* (2021), **vol. 2**, p. 2391.
39. A. Bozbiyik, M. Steinacher, F. Joos, T. F. Stocker, L. Menviel, Fingerprints of changes in the terrestrial carbon cycle in response to large reorganizations in ocean circulation. *Clim. Past* **7**, 319–338 (2011).
40. M. Guillevic *et al.*, Evidence for a three-phase sequence during Heinrich Stadial 4 using a multiproxy approach based on Greenland ice core records. *Clim. Past* **10**, 2115–2133 (2014).
41. P. Köhler, H. Fischer, J. Schmitt, Atmospheric $\delta 13CO_2$ and its relation to pCO_2 and deep ocean δ13C during the late Pleistocene. *Paleoceanography* **25**, PA1213 (2010).
42. L. Menviel, A. Mouchet, K. J. Meissner, F. Joos, M. H. England, Impact of oceanic circulation changes on atmospheric $\delta 13CO_2$. *Global Biogeochem. Cycles* **29**, 1944–1961 (2015).
43. J. Gottschalk *et al.*, Biological and physical controls in the Southern Ocean on past millennial-scale atmospheric CO_2 changes. *Nat. Commun.* **7**, 11539 (2016).
44. L. Skinner, L. Menviel, L. Broadfield, J. Gottschalk, M. Greaves, Southern Ocean convection amplified past Antarctic warming and atmospheric CO_2 rise during Heinrich Stadial 4. *Commun. Earth Environ.* **1**, 23 (2020).
45. A. Burke, L. F. Robinson, The Southern Ocean's role in carbon exchange during the last deglaciation. *Science* **335**, 557–561 (2012).
46. S. Y. Lee, J. C. Chiang, K. Matsumoto, K. S. Tokos, Southern Ocean wind response to North Atlantic cooling and the rise in atmospheric CO_2: Modeling perspective and paleoceanographic implications. *Paleoceanography* **26**, PA1214 (2011).
47. P. Ceppi, Y.-T. Hwang, X. Liu, D. M. W. Frierson, D. L. Hartmann, The relationship between the ITCZ and the Southern Hemispheric eddy-driven jet. *J. Geophys. Res. Atmos.* **118**, 5136–5146 (2013).
48. K. A. Dyez, R. Zahn, I. R. Hall, Multicentennial Agulhas leakage variability and links to North Atlantic climate during the past 80,000 years. *Paleoceanography* **29**, 1238–1248 (2014).
49. G. Marino *et al.*, Agulhas salt-leakage oscillations during abrupt climate changes of the Late Pleistocene. *Paleoceanography* **28**, 599–606 (2013).
50. J. V. Durgadoo, B. R. Loveday, C. J. Reason, P. Penven, A. Biastoch, Agulhas leakage predominantly responds to the Southern Hemisphere westerlies. *J. Phys. Oceanogr.* **43**, 2113–2131 (2013).
51. V. Montade *et al.*, Vegetation and climate changes during the last 22,000 yr from a marine core near Taitao Peninsula, southern Chile. *Palaeogeogr. Palaeoclimatol. Palaeoecol.* **369**, 335–348 (2013).
52. T. Tschumi, F. Joos, M. Gehlen, C. Heinze, Deep ocean ventilation, carbon isotopes, marine sedimentation and the deglacial CO_2 rise. *Clim. Past* **7**, 771–800 (2011).
53. L. C. Menviel *et al.*, Enhanced Southern Ocean CO_2 outgassing as a result of stronger and poleward shifted southern hemispheric westerlies. *Biogeosciences* **20**, 4413–4431 (2023).
54. L. Menviel, P. Spence, Southern Ocean circulation's impact on atmospheric CO_2 concentration. *Front. Marine Sci.* **10**, 1328534 (2024).
55. D. Munday, H. Johnson, D. Marshall, Impacts and effects of mesoscale ocean eddies on ocean carbon storage and atmospheric pCO_2. *Global Biogeochem. Cycles* **28**, 877–896 (2014).
56. C. W. Böning, A. Dispert, M. Visbeck, S. Rintoul, F. U. Schwarzkopf, The response of the Antarctic Circumpolar Current to recent climate change. *Nat. Geosci.* **1**, 864–869 (2008).
57. T. A. Ronge *et al.*, Radiocarbon constraints on the extent and evolution of the South Pacific glacial carbon pool. *Nat. Commun.* **7**, 11487 (2016).
58. E. L. Sikes, A. C. Elmore, K. A. Allen, M. S. Cook, T. P. Guilderson, Glacial water mass structure and rapid δ18O and δ13C changes during the last glacial termination in the Southwest Pacific. *Earth Planet. Sci. Lett.* **456**, 87–97 (2016).
59. G. Siani *et al.*, Carbon isotope records reveal precise timing of enhanced Southern Ocean upwelling during the last deglaciation. *Nat. Commun.* **4**, 2758 (2013).
60. K. Pahnke, R. Zahn, Southern Hemisphere water mass conversion linked with North Atlantic climate variability. *Science* **307**, 1741–1746 (2005).
61. J. Roberts *et al.*, Evolution of South Atlantic density and chemical stratification across the last deglaciation. *Proc. Natl. Acad. Sci. U.S.A.* **113**, 514–519 (2016).
62. T. Chen *et al.*, Synchronous centennial abrupt events in the ocean and atmosphere during the last deglaciation. *Science* **349**, 1537–1541 (2015).
63. O. Lecomte *et al.*, Vertical ocean heat redistribution sustaining sea-ice concentration trends in the Ross Sea. *Nat. Commun.* **8**, 258 (2017).
64. D. Ferreira, J. Marshall, C. M. Bitz, S. Solomon, A. Plumb, Antarctic Ocean and sea ice response to ozone depletion: A two-time-scale problem. *J. Clim.* **28**, 1206–1226 (2015).
65. J. A. Stewart *et al.*, Arctic and Antarctic forcing of ocean interior warming during the last deglaciation. *Sci. Rep.* **13**, 22410 (2023).
66. V. Masson-Delmotte *et al.*, GRIP deuterium excess reveals rapid and orbital-scale changes in Greenland moisture origin. *Science* **309**, 118–121 (2005).
67. B. R. Markle, E. J. Steig, Improving temperature reconstructions from ice-core water-isotope records. *Clim. Past* **18**, 1321–1368 (2022).
68. R. Uemura *et al.*, Asynchrony between Antarctic temperature and CO_2 associated with obliquity over the past 720,000 years. *Nat. Commun.* **9**, 961 (2018).
69. A. Landais *et al.*, Interglacial Antarctic-Southern Ocean climate decoupling due to moisture source area shifts. *Nat. Geosci.* **14**, 918–923 (2021).

70. J. Nusbaumer, T. E. Wong, C. Bardeen, D. Noone, Evaluating hydrological processes in the community atmosphere model version 5 (CAM5) using stable isotope ratios of water. *J. Adv. Model. Earth Syst.* **9**, 949–977 (2017).
71. J. Lynch-Stieglitz *et al.*, Muted change in Atlantic overturning circulation over some glacial-aged Heinrich events. *Nat. Geosci.* **7**, 144–150 (2014).
72. R. Ferrari *et al.*, Antarctic sea ice control on ocean circulation in present and glacial climates. *Proc. Natl. Acad. Sci. U.S.A.* **111**, 8753–8758 (2014).
73. J. W. Rae *et al.*, CO_2 storage and release in the deep Southern Ocean on millennial to centennial timescales. *Nature* **562**, 569–573 (2018).
74. K. C. Martin *et al.*, Bipolar impact and phasing of Heinrich-type climate variability. *Nature* **617**, 100–104 (2023).
75. J. W. Rae *et al.*, Deep water formation in the North Pacific and deglacial CO_2 rise. *Paleoceanography* **29**, 645–667 (2014).
76. M. H. Walczak *et al.*, Phasing of millennial-scale climate variability in the Pacific and Atlantic Oceans. *Science* **370**, 716–720 (2020).
77. L. Herraiz-Borreguero, A. C. Naveira Garabato, Poleward shift of circumpolar deep water threatens the East Antarctic Ice Sheet. *Nat. Clim. Change* **12**, 728–734 (2022).
78. J. Ahn, E. J. Brook, K. Howell, A high-precision method for measurement of paleoatmospheric CO_2 in small polar ice samples. *J. Glacio.* **55**, 499–506 (2009).
79. J. Severinghaus (U.S. Antarctic Program (USAP) Data Center, 2015).
80. M. Sigl *et al.*, The WAIS Divide deep ice core WD2014 chronology–Part 2: Annual-layer counting (0–31 ka BP). *Clim. Past* **12**, 769–786 (2016).
81. T. Fudge, K. C. Taylor, E. D. Waddington, J. J. Fitzpatrick, H. Conway, Electrical stratigraphy of the WAIS Divide ice core: Identification of centimeter-scale irregular layering. *J. Geophys. Res. Earth Surface* **121**, 1218–1229 (2016).
82. M. Etminan, G. Myhre, E. J. Highwood, K. P. Shine, Radiative forcing of carbon dioxide, methane, and nitrous oxide: A significant revision of the methane radiative forcing. *Geophys. Res. Lett.* **43**, 12,614–12,623 (2016).
83. J. Zhu *et al.*, Assessment of equilibrium climate sensitivity of the Community Earth System Model version 2 through simulation of the Last Glacial Maximum. *Geophys. Res. Lett.* **48**, e2020GL091220 (2021).
84. J. W. Hurrell *et al.*, The community earth system model: A framework for collaborative research. *Bull. Am. Meteorol. Soc.* **94**, 1339–1360 (2013).
85. J. Hu, J. Emile-Geay, J. Nusbaumer, D. Noone, Impact of convective activity on precipitation $\delta 18O$ in isotope-enabled general circulation models. *J. Geophys. Res. Atmos.* **123**, 13,595–13,610 (2018).
86. R. Uemura *et al.*, Ranges of moisture-source temperature estimated from Antarctic ice cores stable isotope records over glacial–interglacial cycles. *Clim. Past* **8**, 1109–1125 (2012).
87. B. Stenni *et al.*, The deuterium excess records of EPICA Dome C and Dronning Maud Land ice cores (East Antarctica). *Q. Sci. Rev.* **29**, 146–159 (2010).
88. B. R. Markle *et al.*, Global atmospheric teleconnections during Dansgaard-Oeschger events. *Nat. Geosci.* **10**, 36–40 (2017).
89. W. P. Sijp, M. H. England, The effect of a northward shift in the southern hemisphere westerlies on the global ocean. *Prog. Oceanogr.* **79**, 1–19 (2008).